Proton-Induced Transients and Charge Collection Measurements in a LWIR HgCdTe Focal Plane Array

Paul W. Marshall, John E. Hubbs, Douglas C. Arrington, Cheryl J. Marshall,
Robert A. Reed, George Gee, James C. Pickel, and Rodolfo A. Ramos

***Abstract*---** We compare measurements and modeling of 27 and 63 MeV proton-induced transients in a large-format HgCdTe long wavelength infrared (LWIR) focal plane assembly operating at 40K. Charge collection measurements describe very limited diffusion of carriers to multiple pixels showing significantly reduced particle induced cross-talk for the lateral diffusion structure.

1. INTRODUCTION

Satellite applications for infrared detectors require very low noise performance, even in the presence of charged particles from galactic cosmic rays, trapped protons, and solar energetic particle events. Particle-induced transients have been identified as an important noise source in astronomy applications on ESA's ISO satellite [1], and their impact on infrared imagery has also been observed in NASA's Hubble Space Telescope's NICMOS infrared instrument [2]. Efforts to understand and model the charge deposition and collection processes in modern IR detectors are an important step in preparation for upcoming NASA missions such as the James Webb Space Telescope.

Techniques and tools to analyze particle-induced transient effects have been described in [3, 4, and references therein]. Reference [4] also compares modeled results to measured transient response in two scenarios. One comparison is based on flight data for a HgCdTe array exposed to trapped protons, and the other is for a Si visible imaging array exposed to heavy ions under controlled laboratory conditions. However, to date we know of no report of proton-based testing for transients in modern IR arrays operating under cryogenic conditions, and such data are necessary to understand the charge collection mechanisms and provide relevant benchmarks for modeling techniques. Our study examines proton-induced transients in terms of both magnitude and charge spreading in a long wavelength infrared (LWIR) HgCdTe array and compares the measured response with modeling to assess the relative roles of charge collection by drift and diffusion mechanisms.

2. DEVICE DESCRIPTION

Our test article is a large-format HgCdTe LWIR HgCdTe focal plane assembly with a pixel pitch of 60 μm and a cutoff wavelength exceeding 11 μm. It is a state-of-the-art detector but has not been selected as a flight candidate for any NASA programs. The detectors were grown by molecular-beam epitaxy (MBE) on CdZnTe substrates using a planarized double layer heterojunction design. As depicted in Figure 1, the detectors utilize lateral collection diodes so that only the implanted diode volume relies on charge collection by drift, and charge collection from the surrounding material is due to diffusion charge that reaches the central volume

Paul W. Marshall is a consultant to NASA Goddard Space Flight Center, Brookneal, VA. (pwmarshall@aol.com)
John E. Hubbs and Douglas C. Arrington are with the Air Force Research Laboratory/Space Vehicles Directorate, Infrared Radiation Effects Laboratory, Ball Aerospace & Technologies Corp., Albuquerque, NM
Rudolfo A. Ramos is with the Air Force Research Laboratory/Space Vehicles Directorate, Infrared Radiation Effects Laboratory, Albuquerque, NM
George Gee is with SGT, Inc., Greenbelt, MD.
James C.Pickel is with PRT, Inc., Fallbrook, CA.
Robert A. Reed and Cheryl J. Marshall are with NASA Goddard Space Flight Center, Greenbelt, MD.

This work was supported by NASA Goddard Space Flight Center under the James Webb Space Telescope Program, the NASA Electronic Parts and Packaging Program, and the Defense Threat Reduction Agency Radiation Tolerant Microelectronics Program.

from lateral and from vertical diffusion. The implanted diode has a 14 μm diameter and nominal 1 μm thickness, and the remaining (vast majority) of the pixel volume is considered to be field free.

The small size of the pixel's collection diode would normally result in very poor quantum efficiency. However in our case each pixel incorporates a micro-lens structure to focus light across the spectral band of interest to the pixel's central collection volume. This structure helps solve one of the most troubling problems in producing LWIR detectors since defects located in the pixel's field free regions do not compromise the dark current and operability of the array. Using this structure the detector quantum efficiency is 54% (in the absence of any antireflective coatings) based on measurements of the focal plane output versus photon irradiance. The median pre-irradiation pixel dark current is <0.05 pA at 40 K and the array has excellent responsivity uniformity (sigma/mean ~ 4%). In two separate test trips we evaluated 2 hybridized focal plane arrays (FPAs), both of which were representative of the same technology. Additional details of the device are provided in [5].

Since so little (< 0.2%) of the pixel's volume is actually in depletion, optical detection and collection of signal electrons relies extensively on properties of the field-free region. Diffusion is important in both the vertical and horizontal directions. Optical measurements indicate a lateral collection corresponding to an effective diffusion length of about 16 μm. We expect the vertical collection depth to be on the order of 10 μm as defined by the MBE growth process.

The detector array is indium bump bonded to a CMOS readout integrated circuit (ROIC) which provides for a snapshot mode readout with a frame rate of 100 Hz. The ROIC utilizes a capacitive transimpedance amplifier (CTIA) unit cell with on-chip correlated-double-sampling (CDS). The integration capacitance of 150 fF coupled with the subsequent ROIC gain provides a measured conversion gain of 0.82 μV/electron. The unit cell amplifier is buffered by a source follower that places the pixel outputs into a pipeline architecture where the signal from one row is stored while the output amplifier is reading the signal from the previous row. The output amplifier is also a source follower with an on-chip load. The data acquisition system noise was typically around 120 electrons, and the total read noise for the data reported here was around 200 electrons.

Analog and digital test modes are built in, and both analog and digital monitor points can be read out permitting health checks of the ROIC during radiation testing. For example, threshold shifts of representative FETs, node voltages and various clock lines can be monitored as a function of proton exposure. In addition to the hybrid FPAs, a single copy of a bare CMOS ROIC from the lot used in the FPAs was evaluated for transient response in the absence of the detector array.

3. Experimental Approach

The University of California at Davis Crocker Nuclear Laboratory cyclotron facility [6] provided 27 and 63 MeV protons for transient testing. Beam flux was controlled in real time based on secondary emission monitor currents and these were correlated to Faraday cup current measurements as part of the setup preceding each run sequence. A diagram of the test configuration is provided in Figure 2. Protons were incident at an angle of 45 degrees relative to the plane of the FPA. Protons incident on the FPA thus traversed both the detector array and the ROIC. There was a slight offset in registration of the detector and ROIC unit cells resulting from the tilt, however we do not believe this is significant, especially since we found the vast majority of the ion-induced signal to be due to the detector rather than the ROIC. Reference [5] provides more details of the dewar modifications necessary to accommodate the 45 degree incidence angle while preserving the ability to perform radiometric measurements. The dewar had only one window for proton trajectories, and 45 degrees was the only possible incidence angle.

The array response was evaluated at two proton energies. The cyclotron provided energies of either 63 MeV or 29.9 MeV beam at the beamline exit window. Energy loss calculations show that transport through 5 cm of air, the dewar's 125 μm thick kapton vacuum window, and the two 25 μm Al windows resulted in a proton energy at the DUT of 27 MeV. At 63 MeV the energy loss was negligible.

All data were acquired at 40K using full frame readouts under the lowest possible illumination conditions (note: zero photon flux is not possible

with sensitivity to long wavelength photons). Baseline pixel dark currents were <0.05 pA. Readout timing effects were compared in two separate experiments. One set yielded 100% staring efficiency with integration occurring during readout, and the other set resulted in 50% staring efficiency with an interleaved integrate-then read scheme which resulted in slightly elevated read noise. In both schemes the integration time was maintained at 39.54 ms, and sequences of multiple frames (either 87 or 40) were acquired during each "run". Clear frame sequences were collected prior to each run to allow for baseline subtractions. Beam flux was controlled as a test variable, and frame sequences spanning over 2 orders of magnitude were collected with the lower fluxes less than 5×10^2 protons/cm^2/s. The beam dosimetry in this regime was only good in a relative sense, and does not support the calculation of absolute cross-sections.

The data reported here are all collected under low proton flux conditions so that probabilities of multiple proton strikes in the same portion of the array are negligible. Typically, the hit probability was less than 0.001. The total proton exposure during these tests was well below the levels required to induce any damage to the device, and this was verified with photometric and other tests during and after the transient testing which resulted in less than 10 rads(Si) total.

4. Data Analysis and Results

Data Analysis Algorithms: Data analysis requires considerable efforts to identify valid struck pixels versus either erratic pixels or normal pixels influenced by the background of random noise. Both the clear (without beam) and beam "runs" yield a data "cube" of 87 sequential snapshot frames as depicted in Figure 3. Data are analyzed using the Flexible Image Transfer System (FITS) format and the IDL programming language. The first step involves "scrubbing" to remove aberrant pixels. In this step, each pixel position is interrogated over the entire 87 frames, and flagged for removal from the analysis if anywhere it exhibited readings that are saturated, consistently erratic, or stuck across multiple frames. After scrubbing the data cubes for both the clear condition and the proton run to exclude invalid pixel positions, the average clear value for each individual pixel is subtracted from the corresponding pixel position for each frame in the data run. The resulting scrubbed and background subtracted data cube is then analyzed for noise on both a pixel by pixel and on an array wide basis. Figure 4 presents an example of a typical frame of data that has been scrubbed and background subtracted. The signals have been converted to charge yield using the conversion gain of 0.82 μV/electron. Over the segment of the array presented in the figure, several hits of varying magnitude are apparent, and obviously well separated.

The algorithm used to identify individual hits interrogates each valid pixel position across the sequence of 87 reads. If for any read the value exceeds the defined hit threshold (relative to the noise floor), the reading is flagged as a valid hit, and the surrounding pixels in an 11 x 11 pixel area are analyzed to determine if they also exceed a separately defined threshold. If so, the corresponding signal is noted for that pixel position, and a flag is set to identify the position has been hit. For multiple pixel hits, the center of the hit is determined according to the position of the highest pixel value for the 11 x 11 pixel region. Each valid pixel in each frame is interrogated to obtain a set of valid hits that includes a range of total charge and hit sizes. We note no evidence of hits extending across multiple frames, and this indicates that the transient signatures do not persist through the reset occurring at the beginning of the double correlated sample sequence.

Charge collection and crosstalk: The groups of hits from each run have been examined with various statistical tools to assess the total charge as well as the charge spreading. Figure 5 shows an example histogram based the same data set used to generate Figure 4. Integrating over hits from all 87 frames, with a 27 MeV proton flux estimated at just under 1×10^3 p/cm^2/s, we identify a total of 6,202 hits involving at least one pixel exceeding a 4,000 electrons threshold. The selection of the threshold value is an important factor in determining the total number of hits, and we will explore this in more detail later. For now, we note that above 4,000 electrons the number of events versus total charge declines into broad peak with a peak value at about 7×10^4 electrons.

The stopping power for 27 MeV protons in HgCdTe is 0.01 MeVcm^2/mg, and the ionization potential is approximately 1.04 eV/ion pair. So, considering the 45 degree trajectory, we expect approximately 1.4 x

10^5 ion pairs in the 10 μm MBE layer. For hits central to the diode, since ~90% of the thickness is field free, we expect to collect less than half of that charge, so the "peak" value of 7×10^4 electrons is in good agreement.

As shown in Figure 1, the perimeters of the pixel are not only field free, but are also beyond the 1/e diffusion length of 16 μm, so we expect charge collection from hits near the perimeter to be much less efficient. In addition, hits near the pixel perimeter will be more likely to be shared with neighboring pixels. The result of these two points is that only small charge deposition events are likely from the >50% of the pixel region that is over 16 μm away from the nearest diode implant.

With these issues in mind, we have examined the number of charge deposition events, and their cross-talk characteristics, as a function of cutoff threshold. In Figure 6a and 6b we compare 3-D histograms of all the charge events extracted from the 27 MeV data described in Figures 4 and 5. The format involves stacking all the events by registering the effected neighbors relative to the central hit. The bar heights identify the number of times each position showed higher than expected charge. First we note the general trend of symmetry irrespective of beam trajectory, and the fact that side neighbors are affected more often than corner neighbors. The two figure panels compare results for a central hit threshold of 25,000 electrons, but varying the neighbor hit from 25,000 electrons (part a) to 4,000 electrons (part b). We see just under 2,000 total events and note that each side neighbor is subject to cross-talk in about 2.5% of the hits when neighbors of 25,000 or greater are counted, but this increases to 21% when the neighbor cutoff is decreased to 4,000 electrons. In both cases, we see mostly single pixel events, and note that only 14% of the total hit charge shows up in neighboring pixels (i.e. the crosstalk is 14%). The fact that the neighbor hits are so low in Figure 6a indicates that larger events have the vast majority of their charge located in the hit pixel.

These data are exactly consistent with the view that larger charge deposition hits are spatially correlated with the center of the pixel, and this does not favor charge diffusion to neighbors. In contrast, pixel boundary hits are more likely to be shared with neighboring pixels, but their total charge deposition integrated over all pixels is only a fraction of the charge deposited. In this case, most of the charge is recombined.

In Figure 7 we show the numbers of instances for which a given number of pixels is affected by 27 MeV proton exposure. This analysis considers the same data run as the previous charts, and supplements Figure 6 by indicating the occurrence of hits versus the number of pixels affected. Two curves are plotted. The 25,000 electrons threshold curve corresponds to that charge for the central pixel, but with 4,000 electrons or more for neighbors (as indicated in Figure 6b). The other curve is based on 4,000 electrons cutoffs for both central and neighbor pixels. These data substantiate the claim that charge from larger events is not readily shared, and show that by including the smaller charge events we see many more single pixel events. In both cases, single pixel hits are most likely, followed by double pixel, triple pixel, etc., Note the sharp (expected) drop above 4 pixels which can be described by a hit on a corner boundary. The two curves of Figure 7 match very closely, which indicates that if an event exceeds 4,000 electrons in multiple pixels, then it also exceeds 25,000 electrons. The exception is for single pixel hits for which secondary particles may contribute smaller amounts of charge.

Examining the cross-talk trends versus selection criteria allows us to see that even the smaller charge collection events are qualitatively consistent with our expectations based on charge diffusion in the lateral collection architecture. While we are led to believe that the low charge events are a real consequence of the proton beam environment, we recognize that they are difficult to resolve against random noise and secondary particle events that are encountered during test [7]. We acknowledge that this complicates the job of precisely quantifying both the numbers of pixels affected and amount of charge shared. Even so, the data clearly support the conclusion that the majority of hits deposit most of their charge in only a single pixel.

Proton energy dependence: Tests and analyses identical to those already described, but with a proton energy of 63 MeV, show qualitatively similar results. We do observe trends expected due to the reduced stopping power of the higher energy protons which was 0.0054 $MeVcm^2/mg$. Consequently, each proton hit deposits only half as much charge versus 27 MeV protons and even less total charge is

detected in pixels adjacent to the struck pixel when the hit selection criteria are applied as before.

Figure 8 compares the stacked pixel hits for the 63 MeV tests with the same set of threshold criteria applied in Figure 6. We see 1,200 total events and note that each side neighbor is subject to cross-talk in less than 2% of the hits with the higher cutoff, and the increase is only to 14% with the 4,000 electrons cutoff. The charge showing up in neighbor pixels is, on average, only 11% of the total hit charge. This is roughly consistent to the 14% crosstalk measured for 27 MeV, and we would expect this value to remain constant. Figure 9 shows the results in terms of numbers of neighbors affected with selection criteria for central and neighbor hits as described relative to Figure 7. Note that for 63 MeV protons, which deposit only half as much charge as 27 MeV protons, there are many more events depositing 4,000 electrons in multiple pixels but not as much as 25,000 electrons. We suppose these to be hits near pixel boundaries.

The preceding analyses have assumed that charge sharing between neighboring pixels involves physical relocation of deposited electrons. We recognize there are other mechanisms involving electrical cross-talk and capacitive coupling [8] that can occur, but we consider that these will have relatively small impact compared to the > 10% charge sharing measured for the broad beam geometry experiments described here.

Additional supporting tests: Though over 70 data runs were acquired and analyzed, only 2 have been described here. Results of a two order of magnitude variation over beam flux at each of the two energies were used in an attempt to optimize the signal strength while minimizing problems associated with multiple particles arriving at the same location during the same frame. We did note problems with pileup at the higher fluxes, and insufficient signal at the lowest flux.

Also, separate testing of a bare ROIC was used to discriminate possible readout transient response. Those tests yielded no measurable transients even at beam currents two orders of magnitude above the data analyzed here. Separate testing of another array with the same timing patterns and with the integrate-then-read timing scheme did not show any detectable differences with respect to the cross-talk issue.

5. Discussion and Summary

Practical consequences of charge sharing in this lateral diffusion based structure are especially important in comparison to the expected cross-talk characteristics of the more traditional HgCdTe diode architecture. Typically the entire diode area is covered by a thin (~1 μm) diode with a thicker (~10 μm) field free region underneath, and the IR response relies almost exclusively on vertical diffusion. In comparing our case of 60 μm pitch and 16 μm diffusion length, we see that 78% of the pixel area is within 1 diffusion length of a neighboring pixel's boundary and also its depletion volume. The expected charge sharing from particle transients consequently approaches 100% in the sense that nearly every hit will involve multiple pixels. For the lateral collection device we tested, whether we use number of pixels or amount of charge as a metric, our measurements indicate less than 15% cross-talk in all cases. Consequently, we recognize the lateral collection approach as a tremendous advantage in this regard, and the number of corrupted pixels due to particle strikes should be reduced substantially.

References

1. A.Claret, H.Dzitko, and J.J.Engelmann, "Transient Particle Effects on the ISOCAM Instrument On-board the Infrared Space Observatory," IEEE Trans. Nucl. Sci., Vol. 49, p. 1511, Dec. 1999.
2. R.Ladbury, J.C.Pickel, G.Gee, T.M.Jordan, L.Bergeron, B.Rauscher, R.A.Reed, P.W.Marshall, D.Figer, B.Fodness and S.Kniffen, "Characteristics of the Hubble Space Telescope's Radiation Environment Inferred from Charge Collection Modeling of Near-Infrared Camera and Multi-Object Spectrometer Darkframes," IEEE Trans. Nucl. Sci., Vol. 49, p. 2765, Dec. 2002.
3. T.E.Dutton, W.F.Woodward and T.S.Lomheim, "Simulation of Proton-Induced Transients on Visible and Infrared Focal Plane Arrays in a Space Environment, SPIE, Vol. 3063, p.77, 1997.
4. J.C.Pickel, R.A.Reed, R.Ladbury, B.Rauscher, P.W.Marshall, T.M.Jordan, B.Fodness and G.Gee, "Radiation-Induced Charge Collection in Infrared Detector Arrays," IEEE Trans. Nucl. Sci., Vol. 49, p. 3822, Dec. 2002.
5. John E. Hubbs, Douglas C. Arrington, Mark E. Gramer, Gary A. Dole, Rodolfo A. Ramos, "Proton

and Total Dose Radiation Characterization of VLWIR Staring Focal Plane Arrays with Micro-Lens Detectors," Proceedings of the 2003 Meeting of the MSS Specialty Groups on Infrared Detectors, Tucson, Arizona, February 2003.

6. C.M. Castaneda, "Crocker Nuclear Laboratory (CNL) Radiation Effects Measurement and Test Facility", 2001 IEEE Radiations Effects Data Workshop, pp 77-81, IEEE (2001).

7. J.C. Pickel, R.A. Reed, P.W. Marshall, T.M. Jordan, G. Gee, A. Waczynski, E. Polidan, S. Johnson, B. Fodness, M. McKelvey, R.E. McMurray, K.A. Ennico, R.R. Johnson, and C. McCreight, "Proton-Induced Secondary Particle Environment for Infrared Sensor Applications," in this journal.

8. Andrew C. Moore, Zoran Ninkov, and William Forrest, "Interpixel capacitance in non-destructive focal plane arrays," Proceedings of the SPIE, Volume 5167, paper 26, July, 2003.

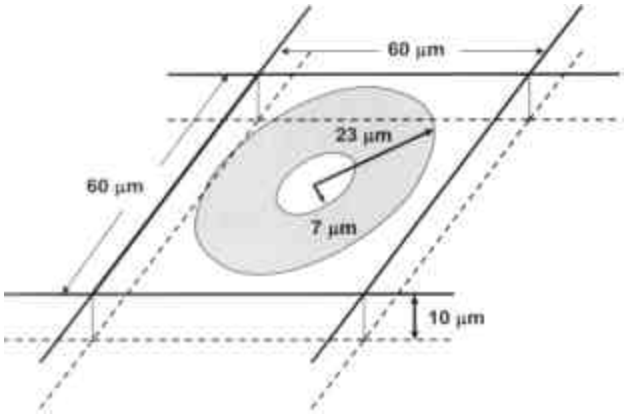

Figure 1. The 60 μm unit cell utilizes a central implanted diode structure and both vertical and lateral charge collection via diffusion with an effective diffusion length of about 16 μm. The diode's depletion has a 7 μm radius and is approximately 1 μm thick. Over 99.8% of the pixel volume is field-free resulting in low dark currents.

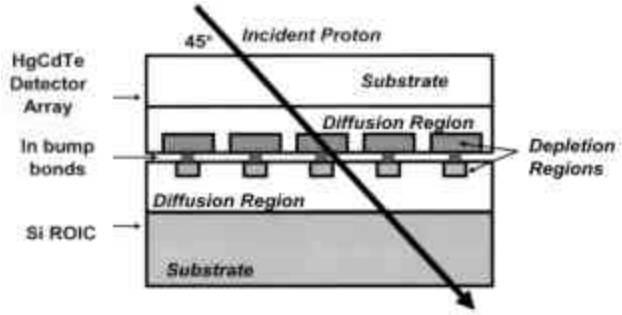

Figure 2. The LWIR FPA orientation to the beam line resulted in 45 degree traversal so that the detector array and read out integrated circuit (ROIC) both intercepted protons. Note that the figure is not drawn to scale, and actual depletion regions were very small in both the detector and in the ROIC.

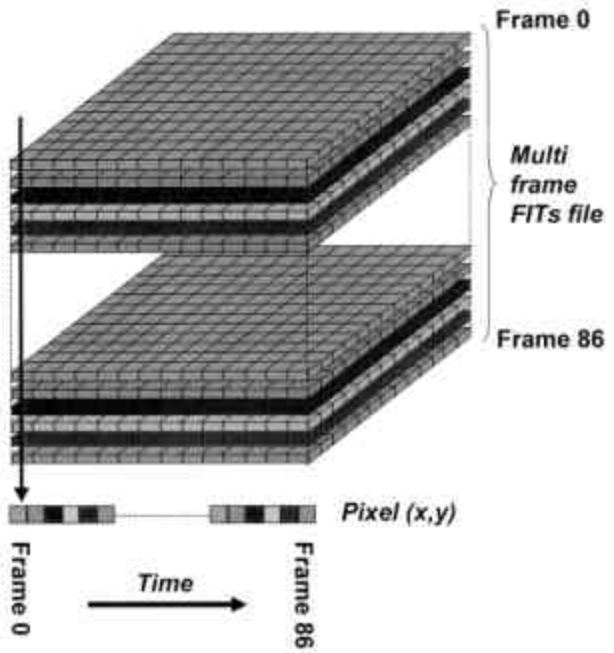

Figure 3. Each run yields a data "cube" comprised of 87 sequential snapshot reads stored in a Flexible Image Transfer System (FITS) format. Data are "scrubbed" to remove aberrant pixels before identifying valid transients.

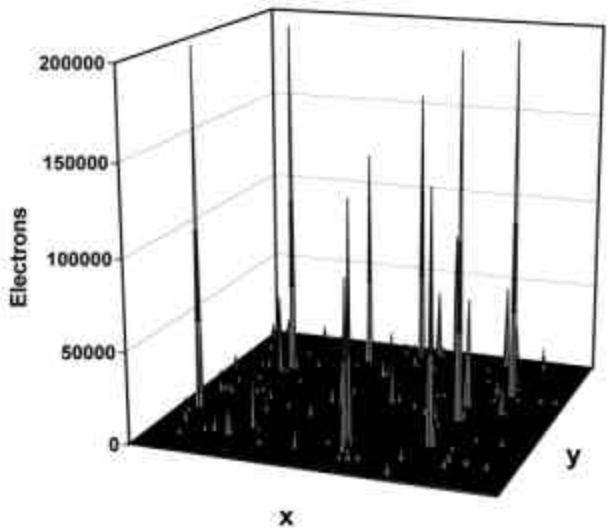

Figure 4. This frame segment of "typical" data showing 27 MeV proton hits has been scrubbed for erratic pixels and background subtracted. Single particle hits are well separated and vary in amplitude.

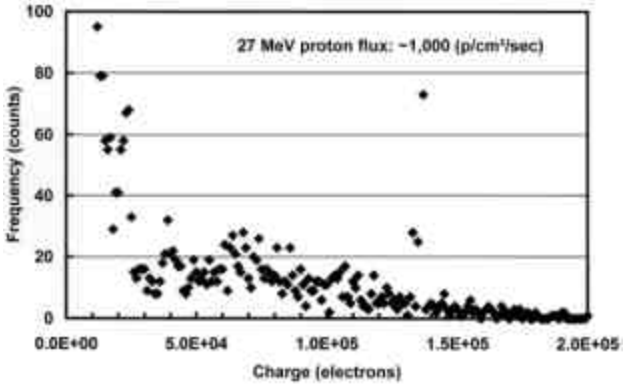

Figure 5. This representative charge histogram shows the hit frequency after integrating the total charge associated with a hit, irrespective of the number of pixels affected. Events around 70,000 electrons are expected based on proton LET and device thickness.

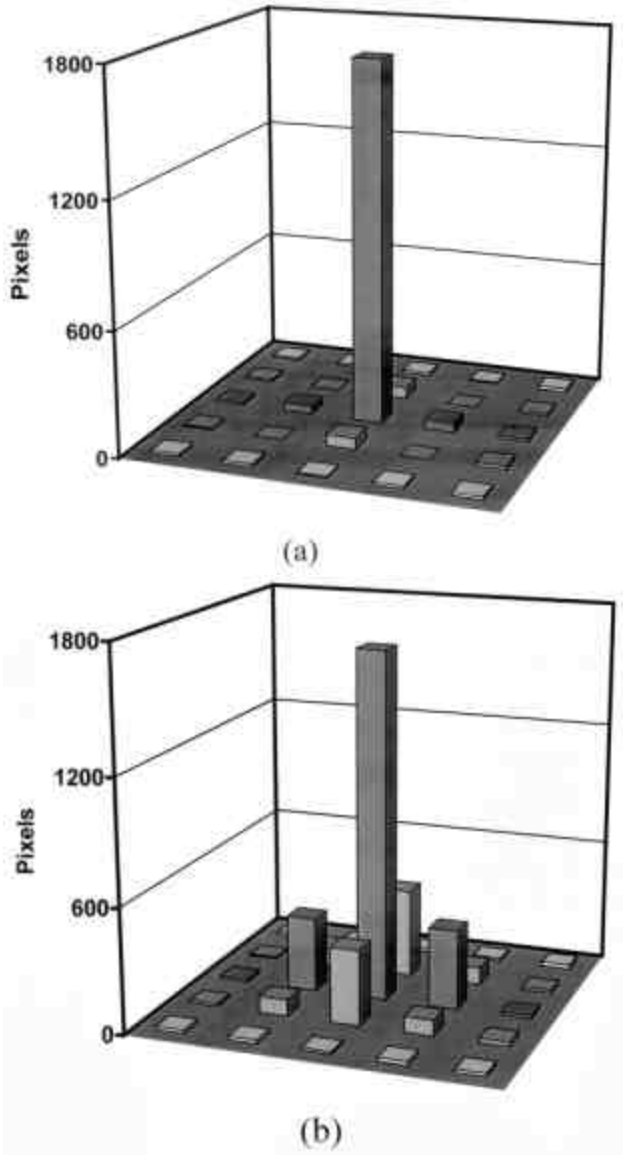

Figure 6. These stacked plots are for 27 MeV protons. Part A corresponds to hits with 25,000 or more electrons and shows the same total events but less cross-talk than part b which corresponds to central hits greater than 25,000 electrons and includes neighbor hits with 4,000 or more electrons.

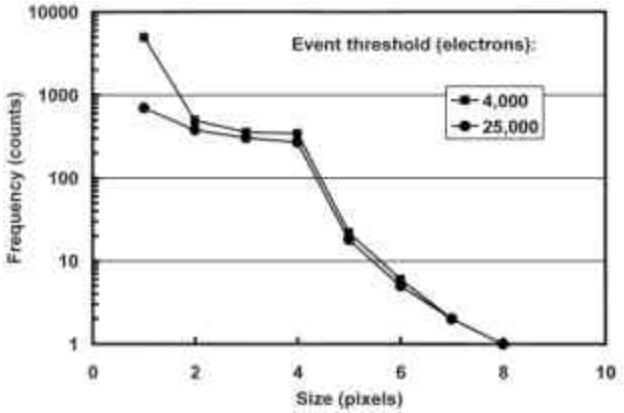

Figure 7. Histograms for 27 MeV protons hits show the number of pixels affected versus hit size. Larger events are limited to relatively few pixels.

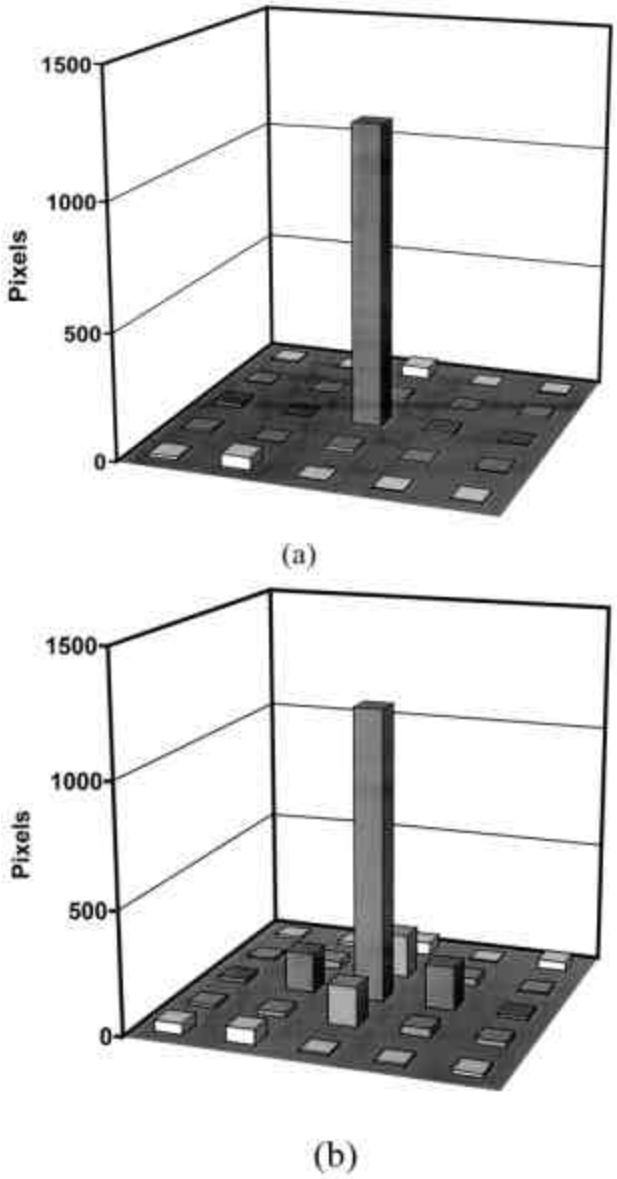

Figure 8. These stacked plots are for 63 MeV protons. Both parts correspond to center pixel hits with 25,000 or more center hit electrons, but as in Figure 6b, including neighbor events of 4,000 or more electrons increases the pixel cross-talk.

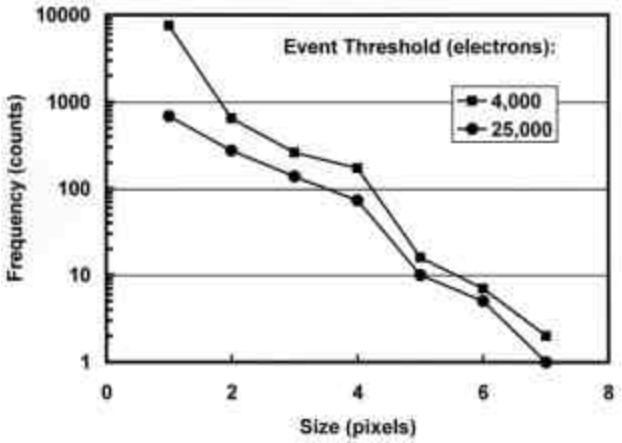

Figure 9. Histograms for 63 MeV protons hits show the number of pixels affected versus hit size. Larger events are limited to relatively few pixels.